Remote Sensing of Environment 273 (2022) 112965

Contents lists available at ScienceDirect

Remote Sensing of Environment

journal homepage: www.elsevier.com/locate/rse

Characterization of tephra deposits using VNIR and MIR spectroscopy: A comprehensive terrestrial tephra spectral library

C.J. Leight [a,*], Molly C. McCanta [a], Timothy D. Glotch [b], Bradley J. Thomson [a], Cheng Ye [c], M. Darby Dyar [d,e]

[a] Department of Earth and Planetary Sciences, University of Tennessee, 1621 Cumberland Avenue, Knoxville, TN 37996, United States of America
[b] Department of Geosciences, Stony Brook University, 255 Earth and Space Science Building, Stony Brook, NY 11794, United States of America
[c] Department of Astronomy and Planetary Science, Northern Arizona University, 527 S. Beaver St., Flagstaff, AZ, United States of America
[d] Planetary Science Institute, 1700 East Fort Lowell, Suite 106, Tucson, AZ 85719, United States of America
[e] Department of Astronomy, Mount Holyoke College, 50 College St., South Hadley, MA 01075, United States of America

ARTICLE INFO

Editor: Jing M. Chen

Keywords:
Spectral library
Tephra
Visible near-infrared (VNIR)
Mid-infrared (MIR)
Spectroscopy
Volcanics

ABSTRACT

Laboratory spectral libraries of well-characterized natural samples are necessary for accurate interpretation of remote sensing spectral data. Tephra deposits, the result of explosive volcanic eruptions, are potentially found on all differentiated terrestrial bodies and are important chronologic and compositional marker beds on Earth. Here we present a visible/near-infrared (VNIR, 0.35–2.5 μm) and mid-infrared (MIR, 3.5–25 μm) spectral library composed of nineteen natural tephra samples from ten volcanic sources that span a range of compositions and components. The bulk, glass, and mineral phase compositions of each sample are measured and spectra from multiple size fractions of each sample were collected. The library can be found via the Terrestrial Analog portal (DOI: https://doi.org/10.5066/P9O54M4Q).

1. Introduction

At Earth's surface pressure and temperature conditions, explosive eruptions are common. Less than one weight percent of volatile elements entrained in a magma can lead to explosive eruptions (e.g., Parfitt and Wilson, 1995). On bodies with lower atmospheric pressure or no atmosphere at all, even smaller amounts of magmatic volatiles are needed to produce an explosive eruptive phase. Potential evidence of explosive eruptions on numerous other planetary bodies has been observed, including on Mars (e.g., Hynek et al., 2003; Mandt et al., 2008), the Moon (e.g., Wilson and Head III, 1981; Gaddis et al., 1985), and Mercury (e.g., Head et al., 2008; Kerber et al., 2011; Goudge et al., 2014). Extraterrestrial explosive volcanic samples also have been returned by the Apollo missions in the form of glass beads that are interpreted to have formed during pyroclastic eruptions at the lunar surface (e.g., Heiken et al., 1974; Pieters et al., 1974; Fogel and Rutherford, 1995).

Tephra are composed of a heterogeneous mix of mineral fragments, glass, and debris from previous eruptions. Due to their geologically instantaneous deposition over large areas, they often serve as terrestrial geochronologic markers (Brown et al., 1992; Trepte and Hitchman, 1992; van den Bogaard et al., 1994; Lowe, 2011). Additionally, the glass component of tephra deposits, formed via the rapid quenching of melts during eruption, is often used diagnostically to define layers as volcanic in mixed-source materials and to constrain their volcanic source (e.g., Carter et al., 1995; Shane, 2000; Lowe, 2011; Cassidy et al., 2014).

For bodies other than Earth, or for large or remote locations anywhere in the Solar System, spectral identification remains the primary method to remotely characterize surface composition. Infrared spectroscopy is also a non-destructive method for characterizing samples in the laboratory. Infrared spectra can provide positive identifications of silicate materials without requiring physical contact with a sample and are regularly used to evaluate the compositions of planetary surfaces (e.g., Hunt, 1979; Clark et al., 2003; Hook et al., 2005), but amorphous materials present challenges to such identifications. Unfortunately, the inherent compositional and structural complexities in glass introduce ambiguities when interpreting spectra from layers of potential volcanic origin because glass typically has only a few, broad infrared spectral features (e.g., Adams and McCord, 1971; Minitti et al., 2002; Dalby and King, 2006). To date, the effect of glass on infrared spectra has been constrained largely using synthetic glasses and mineral mixtures to

* Corresponding author.
E-mail address: cleight@utk.edu (C.J. Leight).

https://doi.org/10.1016/j.rse.2022.112965
Received 23 July 2021; Received in revised form 2 February 2022; Accepted 19 February 2022
Available online 5 March 2022

Table 1
Samples, sample abbreviations, locality, size fractions, and general composition. Eruption dates are noted when known. Petrologic classifications determined from total alkali vs silica plot (Fig. 1) of bulk wt% SiO_2 (Table 2).

Sample	Abbreviation	Locality	Size Fractions	Petrologic Classification
Cima 1	Cima1	Cima Volcanic field, Mojave Desert, CA	B	Basalt
Cima 3	Cima3	Cima Volcanic field, Mojave Desert, CA	B	Basalt
Crater Flats Unit 1	CFU1	Crater Flats Volcanic field, Nevada	A	Trachy-Basalt
Crater Flats Unit 2	CFU2	Crater Flats Volcanic field, Nevada	A	Trachy-Basalt
Crater Flats Unit 4	CFU4	Crater Flats Volcanic field, Nevada	A	Basalt
Crater Flats Southwest Little Cone	CFSW	Crater Flats Volcanic field, Nevada	A	Trachy-Basalt
Heimaey	Hei	Heimaey Island (1973)	B	Trachy-Basalt
Vesuvius	Ves	Mount Vesuvius, Campania, Italy (1631)	A	Tephry-phonolite
Summerland Sample 1	SS1	Mt. Rainier, WA	A	Basaltic Andesite
Summerland Sample 2	SS2	Mt. Rainier, WA	A	Basaltic Andesite
Summerland Sample 3	SS3	Mt. Rainier, WA	A	Basaltic Andesite
Summerland Sample 4	SS4	Mt. Rainier, WA	A	Trachy Andesite
R8D1	R8D1	Mt. Rainier, WA	A	Andesite
Okmok Ashishik Point	OAP	Okmok volcano, Aleutian Islands, AK	A	Dacite
Pinatubo S2	PS2	Mt. Pinatubo, Philippines (1991)	A	Dacite
Pinatubo S3	PS3	Mt. Pinatubo, Philippines (1991)	A	Rhyolite
Hotlum Ash	HLA	Mt. Shasta, CA	A	Andesite
Mount St. Helens	MSH	Mt. St. Helens, WA (1980)	A	Rhyolite
Bishop Tuff	BT	California	A	Rhyolite

*Size fractions:
A - >, 250 μm–2 mm, 125–250 μm, 63–125 μm, <63 μm
B - > 250–500 μm 125–250 μm, 63–125 μm, <63 μm

mimic varying sample compositions and phase assemblages (e.g., Minitti et al., 2002; Horgan et al., 2014; Dufresne et al., 2009; Cannon et al., 2017).

Natural tephra samples present unique challenges in that they contain a heterogeneous amalgamation of glass, minerals, and debris from previous eruptions. Glass-mineral mixtures in natural samples are more geologically relevant than glass alone. Therefore, accurate remote identification of rocks and minerals is predicated on well-characterized laboratory sample libraries for comparison to field or remote sensing spectra. In this paper, we present and summarize a spectral library of natural tephra samples that encompass the compositional range of terrestrial explosive volcanic compositions. Because bulk weight % (wt %) SiO_2 is the basis for characterizing different magma types, and correlates with variations in other oxide abundances, the SiO_2 composition of the samples is emphasized. The library covers both VNIR (0.35–2.5 μm) and MIR (3.5–25 μm) spectral regions and utilizes 19 samples ranging in composition from basaltic to rhyolitic, including alkaline endmembers.

2. Library assembly and characterization methodology

2.1. Tephra library source materials

The tephra spectral library contains 19 samples from ten different terrestrial locations (Table 1) that span a wide range of bulk compositions, glass compositions, and mineral types and abundances (Tables 2, 3, and 4, respectively, and Fig. 1). When sampled (Sup.Table 1), care was taken to collect interior, non-altered samples. The variety of locations also provides a range of potential weathering grades; seven samples come from the arid Mojave Desert (Cima1, Cima3, CFU1, CFU4, CFU4, CFSW), two come from arctic environments (OAP, Hei), ten come from temperate to tropical environments (Ves, SS1, SS2, SS3, SS4, R8D1, PS2, PS2, HLA, BT), and one (MSH) was collected immediately after eruption before weathering could occur.

2.2. Sample preparation and measurement techniques

Tephra samples were ground by hand under ethanol, dried, and sieved into a variety of size fractions: 250 μm–2 mm or 250–500 μm, 125–250 μm, 63–125 μm, and < 63 μm (Table 1). Size fractions were used to address particle size effects in the spectra, which are most prominent in the MIR, but also exist in the VNIR (Gaffey et al., 1993; Mustard and Hays, 1997). For each sample, a portion of the 125–250 μm size fraction, approximately 0.05 g, was cast into polished epoxy plugs to provide a random sampling of the minerals and glass present in the deposit. Aliquots (~1 g) of each tephra sample were experimentally fused in the lab to determine the bulk chemistry of the sample. The bulk composition beads were then cast into polished epoxy plugs for analysis.

2.2.1. SEM analysis

Polished sample plugs were imaged in backscatter (BSE) mode using the Phenom Pro XL scanning electron microscope (SEM) at the University of Tennessee. BSE images taken at 310–350× magnification under low vacuum with a voltage of 15 kV were used to estimate the crystal abundance of each sample (Table 4). Minor alteration phases, if observed, were included in the phase assemblage because they would affect the spectra; however, no significant alteration phases were observed for any sample. For samples with a glassy groundmass (e.g., CFU1 in Fig. 1), particles entrained in the groundmass with any dimension measuring over 100 μm were counted; each particle of glass+mineral was counted as a particle of glass. Other samples (e.g., R8D1 in Fig. 1) had more pumaceous glass that was separate or welded to a single mineral grain, in which case the glass and mineral were counted as two separate particles. Roughly 500 particles per sample were characterized as glass or mineral type following the methods of McCanta et al. (2015) and Cassidy et al. (2014).

2.2.2. Electron microprobe analysis

Sample plugs were carbon-coated for electron probe microanalysis (EPMA) on the University of Tennessee Cameca SX-100 electron probe. Compositional data were obtained using natural mineral standards for calibration and a 15 kV acceleration voltage. Spot size varied depending on the target material. For glass analyses, a defocused beam resulting in a larger spot size (10 μm) was used to reduce electron beam-induced loss of sodium and other volatile elements and to minimize sample alteration. Areas with low glass abundance and/or high microlite (<10 μm diameter crystals) abundance could not be analyzed using the larger spot size. In these cases, a more focused beam (3 μm spot size) was used, resulting in minor, localized destruction of the sample. A sodium loss routine was run for all glass analyses to account for beam-induced volatile loss (Nielsen and Sigurdsson, 1981). To define glass composition, a minimum of 15 points was averaged together to account for natural

Table 2
Sample bulk compositions.

	CFU4		Cima1		Cima3		CFU1		CFSW		Hei		CFU2	
SiO_2	46.99	(0.84)	48.17	(0.91)	48.65	(0.73)	48.78	(0.47)	48.81	(0.37)	49.54	(0.86)	49.54	(0.92)
$Al2O_3$	16.57	(0.35)	13.51	(1.74)	12.62	(1.66)	16.46	(0.41)	16.39	(0.39)	16.30	(0.71)	17.33	(1.08)
FeO	9.70	(0.20)	9.95	(0.70)	10.73	(0.96)	9.94	(0.51)	9.73	(0.42)	12.44	(0.69)	9.12	(0.79)
MgO	4.69	(0.10)	8.12	(1.10)	11.35	(1.18)	5.08	(0.33)	4.65	(0.22)	3.55	(0.22)	4.77	(0.47)
CaO	9.70	(0.12)	10.61	(0.71)	8.45	(0.50)	8.45	(0.18)	9.12	(0.19)	7.25	(0.18)	8.30	(0.29)
Na_2O	2.87	(0.09)	3.51	(0.34)	3.24	(0.34)	3.29	(0.08)	3.38	(0.12)	4.84	(0.17)	3.65	(0.16)
K_2O	1.64	(0.06)	1.27	(0.17)	1.31	(0.21)	1.88	(0.10)	2.26	(0.11)	1.37	(0.07)	2.02	(0.14)
TiO_2	1.96	(0.06)	2.39	(0.33)	2.00	(0.22)	2.03	(0.08)	2.12	(0.10)	2.79	(0.33)	1.82	(0.26)
P_2O_5	1.23	(0.04)	0.57	(0.09)	0.52	(0.07)	1.37	(0.06)	1.44	(0.11)	0.74	(0.07)	1.23	(0.23)
MnO	0.17	(0.01)	0.18	(0.02)	0.19	(0.02)	0.17	(0.01)	0.17	(0.02)	0.26	(0.02)	0.16	(0.01)
Total	96.40	(1.28)	98.51	(0.35)	99.38	(0.27)	98.03	(0.55)	98.46	(0.24)	99.41	(0.37)	97.95	(1.00)
	Ves		SS1		SS2		SS3		HLA		R8d1		SS4	
SiO_2	50.94	(1.34)	53.77	(0.56)	56.89	(0.49)	56.37	(1.90)	57.46	(2.01)	60.32	(0.38)	60.44	(2.55)
$Al2O_3$	19.82	(0.68)	24.70	(0.23)	22.18	(0.22)	21.58	(0.64)	24.92	(1.59)	20.30	(0.28)	18.06	(2.38)
FeO	5.20	(0.51)	6.83	(0.43)	4.62	(0.27)	5.23	(0.89)	3.60	(0.82)	4.95	(0.23)	5.37	(1.15)
MgO	1.56	(0.23)	2.22	(0.05)	2.43	(0.11)	2.49	(0.24)	3.92	(0.99)	2.02	(0.06)	1.69	(0.46)
CaO	6.67	(0.83)	6.08	(0.17)	6.38	(0.10)	5.92	(0.38)	4.94	(0.70)	5.50	(0.13)	5.21	(0.98)
Na_2O	4.54	(0.15)	3.34	(0.17)	3.68	(0.09)	4.12	(0.25)	2.71	(0.35)	3.55	(0.15)	3.99	(0.30)
K_2O	7.57	(0.40)	0.89	(0.04)	1.26	(0.05)	1.47	(0.14)	0.99	(0.12)	1.60	(0.07)	3.10	(0.36)
TiO_2	0.63	(0.07)	1.56	(0.07)	1.54	(0.12)	1.75	(0.27)	0.91	(0.20)	1.40	(0.06)	0.81	(0.40)
P_2O_5	0.84	(0.47)	0.23	(0.06)	0.16	(0.04)	0.30	(0.14)	0.06	(0.03)	0.17	(0.04)	0.48	(0.20)
MnO	0.15	(0.02)	0.07	(0.01)	0.08	(0.01)	0.08	(0.01)	0.10	(0.02)	0.08	(0.01)	0.09	(0.02)
Total	98.37	(1.39)	99.78	(0.74)	99.26	(0.53)	99.37	(2.06)	99.80	(0.84)	99.91	(0.40)	99.25	(0.85)
	PS2		OAP		PS3		BT		MHS					
SiO_2	67.56	(0.97)	68.51	(0.92)	70.79	(3.51)	73.46	(1.83)	74.03	(2.43)				
$Al2O_3$	15.31	(0.43)	14.98	(0.78)	16.70	(1.86)	15.18	(1.28)	13.32	(1.77)				
FeO	3.06	(0.26)	5.00	(0.65)	1.62	(0.56)	0.93	(0.18)	3.00	(1.85)				
MgO	2.20	(0.10)	0.76	(0.23)	1.18	(0.50)	0.39	(0.12)	1.00	(0.90)				
CaO	4.37	(0.21)	2.76	(0.30)	3.16	(0.89)	1.11	(0.19)	2.09	(0.31)				
Na_2O	3.98	(0.22)	3.49	(0.14)	4.23	(0.15)	2.79	(0.20)	3.86	(0.36)				
K_2O	2.04	(0.09)	3.27	(0.13)	2.51	(0.18)	4.33	(0.26)	2.24	(0.19)				
TiO_2	0.40	(0.06)	0.63	(0.05)	0.20	(0.14)	0.10	(0.03)	0.54	(0.31)				
P_2O_5	0.20	(0.08)	0.18	(0.03)	0.10	(0.15)	0.03	(0.01)	0.11	(0.08)				
MnO	0.09	(0.01)	0.16	(0.03)	0.06	(0.03)	0.05	(0.01)	0.05	(0.03)				
Total	99.45	(0.60)	99.77	(0.35)	100.60	(1.18)	98.51	(1.41)	100.28	(0.83)				

heterogeneities in the glass. Mineral phase compositions were also constrained in this way (supplementary file).

2.2.3. VNIR analysis

An OreXpress spectrometer equipped with a contact probe (1 cm spot size) was used to gather VNIR (350–2500 nm, with 1 nm sampling) reflectance spectra of each sample size fraction at the University of Tennessee. Loose sample was poured onto weighing paper, and gently pressed with a second piece of weighing paper so that the grains formed a flat surface. The spectra were collected in a dark room with all fluorescent lights off and screens angled away from the samples. The contact probe was held vertically to the sample surface, giving incidence and emergence angles of $i = 0°$ and $e = 28°$, respectively. The white reference used is PTFE (polytetrafluoroethylene), and the white references were taken before each sample, with all size fractions collected in a single calibration of the spectrometer, in quick succession. Because PTFE is not a perfect reflective surface, the data were corrected for the presence of PTFE features near 2.2 μm by multiplying the spectra by the reflectance spectrum of a Spectralon reference.

2.2.4. MIR analysis

Bulk MIR (400–2500 cm^{-1}, or 4–25 μm) emissivity spectra were obtained using a Nicolet 6700 FTIR spectrometer at Stony Brook University. Samples were poured into sample cups, heated to 80 °C for at least two hours to remove adsorbed water, then placed in a sample chamber that was cooled to 10 °C. The samples were maintained at 80 °C during measurement. The chamber and the spectrometer were purged using gas scrubbed of H_2O and CO_2 to minimize absorption features, which appear at wavelengths below 8 μm and longer than 12 μm (Ramsey and Christensen, 1998). For each sample, a total of 128 scans at 2 cm^{-1} spectral sampling were averaged and converted to calibrated radiance using two measurements of a custom-built blackbody target heated to 70 °C and 100 °C. Calibrated radiance spectra were further processed to emissivity following the methods in Ruff et al. (1997) and using emissivity calibration routines available in the Davinci software package (http://davinci.asu.edu/).

2.3. Library availability

The library may be found at https://doi.org/10.5066/P9O54M4Q. Each spectrum has a unique name containing the spectral region (VNIR or MIR), sample, and size fraction. Spectral data are stored in two .csv files, one for each spectral region. Compositional information for each spectrum is recorded in .csv files, one for the MIR and one for the VNIR, though compositional information for each sample is identical.

3. Results and discussion

3.1. Glass and bulk compositional results

Bulk compositions of the samples range from 46 to 74 wt% SiO_2, and 4.2–12 wt% total alkali ($Na_2O + K_2O$) (Fig. 2, Table 2). Glass compositions of the samples range from 46 to 80 wt% SiO_2, and 5–15 wt% total alkali ($Na_2O + K_2O$), and the concentrations of glass within the tephra samples range from 40 to 91% of the phase assemblage (Fig. 2, Table 3). This covers the range of inferred extraterrestrial tephra compositions, which are thought to be predominantly basaltic (Delano, 1986; Wilson and Head III, 1994), but with a few localities potentially more felsic (e.

Table 3
Sample glass compositions.

	Hei		CFSW		CFU4		CFU1		Cima3		CFU2		Ves	
SiO_2	49.89	(0.27)	50.17	(0.36)	51.25	(0.57)	51.40	(0.84)	52.53	(1.16)	53.47	(0.86)	53.52	(1.72)
$Al2O_3$	14.43	(0.21)	15.17	(0.69)	13.96	(0.43)	14.19	(1.53)	17.19	(0.72)	13.52	(0.65)	21.46	(0.80)
FeO	13.91	(0.20)	10.15	(0.36)	11.43	(0.40)	11.10	(2.14)	7.44	(0.67)	10.64	(0.91)	4.93	(0.71)
MgO	3.26	(0.09)	4.36	(0.96)	3.90	(0.25)	2.90	(0.76)	2.70	(0.62)	2.34	(0.33)	0.71	(0.20)
CaO	7.16	(0.07)	7.92	(0.64)	7.84	(0.36)	7.86	(1.31)	5.08	(1.08)	6.90	(1.10)	4.98	(0.97)
Na_2O	4.37	(0.57)	4.27	(0.24)	3.13	(0.25)	3.48	(0.46)	5.21	(0.55)	3.68	(0.29)	7.31	(0.88)
K_2O	1.81	(0.09)	3.16	(0.47)	2.78	(0.17)	3.27	(0.84)	5.13	(0.92)	3.81	(0.51)	6.13	(0.95)
TiO_2	3.29	(0.10)	2.55	(0.22)	2.80	(0.10)	3.15	(0.60)	2.99	(0.18)	3.44	(0.34)	0.56	(0.06)
P_2O_5	0.91	(0.03)	1.52	(0.18)	1.71	(0.12)	1.86	(0.43)	1.31	(0.09)	1.76	(0.59)	0.27	(0.34)
MnO	0.32	(0.02)	0.20	(0.02)	0.21	(0.02)	0.20	(0.04)	0.16	(0.03)	0.24	(0.04)	0.17	(0.04)
Total	99.39	(0.59)	99.49	(0.67)	99.03	(0.85)	99.42	(1.52)	99.76	(1.08)	99.80	(1.01)	100.09	(3.63)
	Cima1		SS4		SS3		R8D1		SS1		OAP		SS2	
SiO_2	54.43	(1.38)	57.81	(0.92)	57.94	(3.21)	58.50	(1.12)	60.33	(1.94)	66.75	(2.74)	69.18	(1.24)
$Al2O_3$	17.93	(1.04)	18.33	(0.90)	21.28	(4.51)	18.93	(2.52)	17.12	(1.27)	16.33	(2.86)	14.23	(0.99)
FeO	7.24	(1.46)	6.44	(0.40)	4.63	(2.43)	5.78	(1.46)	6.10	(0.55)	4.50	(1.11)	4.10	(0.35)
MgO	2.32	(0.65)	3.55	(0.24)	2.19	(1.75)	2.84	(0.90)	2.74	(0.74)	0.60	(0.18)	0.95	(0.12)
CaO	4.84	(1.30)	6.75	(0.38)	7.90	(2.34)	6.77	(1.14)	5.97	(0.85)	2.98	(1.33)	3.08	(0.52)
Na_2O	4.50	(0.62)	3.76	(0.32)	4.25	(0.63)	4.16	(0.54)	3.91	(0.38)	4.99	(0.48)	4.51	(0.21)
K_2O	5.35	(1.66)	1.50	(0.21)	1.13	(0.73)	1.38	(0.46)	1.86	(0.35)	2.93	(0.63)	3.13	(0.20)
TiO_2	2.84	(0.40)	1.02	(0.05)	0.77	(0.48)	0.98	(0.29)	1.18	(0.17)	0.57	(0.13)	1.10	(0.09)
P_2O_5	1.41	(0.35)	0.32	(0.03)	0.26	(0.15)	0.31	(0.08)	0.35	(0.04)	0.17	(0.05)	0.28	(0.08)
MnO	0.15	(0.05)	0.12	(0.02)	0.08	(0.05)	0.10	(0.03)	0.11	(0.02)	0.13	(0.03)	0.07	(0.02)
Total	101.05	(0.92)	99.64	(1.06)	100.45	(2.32)	99.78	(1.88)	99.68	(0.79)	99.97	(1.53)	100.65	(1.22)
	HLA		BT		PS3		PS2		MSH					
SiO_2	73.63	(2.40)	75.09	(0.96)	75.84	(2.22)	76.82	(1.66)	79.20	(0.60)				
$Al2O_3$	13.22	(1.04)	12.42	(0.18)	14.16	(1.41)	12.89	(0.40)	12.13	(0.32)				
FeO	1.94	(0.47)	0.66	(0.04)	0.92	(0.31)	0.82	(0.10)	1.60	(0.05)				
MgO	0.45	(0.78)	0.04	(0.01)	0.48	(0.65)	0.22	(0.06)	0.20	(0.02)				
CaO	1.87	(1.21)	0.43	(0.03)	1.22	(0.32)	1.14	(0.07)	0.92	(0.09)				
Na_2O	4.09	(0.31)	3.27	(0.21)	4.14	(0.25)	2.63	(0.88)	2.57	(0.30)				
K_2O	2.76	(0.98)	5.20	(0.22)	3.02	(0.20)	3.11	(0.16)	2.86	(0.09)				
TiO_2	0.79	(0.22)	0.07	(0.02)	0.18	(0.10)	0.14	(0.03)	0.38	(0.04)				
P_2O_5	0.13	(0.08)	0.02	(0.01)	0.04	(0.02)	0.03	(0.01)	0.04	(0.01)				
MnO	0.03	(0.02)	0.03	(0.01)	0.04	(0.01)	0.03	(0.02)	0.03	(0.02)				
Total	98.93	(0.61)	97.24	(1.18)	100.06	(2.87)	97.84	(1.81)	99.95	(0.95)				

Table 4
Sample phase assemblages, as constrained via point counting of epoxy rounds contain a portion of the 125–250 μm size fraction of each sample, described in Section 2.2.1. No phases observed are excluded from count; alteration phases, if observed, are included in the phase assemblage.

Sample	Glass	Pyroxene	Feldspar	Olivine	Apatite	Quartz	Oxide	Total
Cima1	46	9	38	5	1	0	2	100
Cima3	40	24	26	7	0	0	2	100
CFU1	60	4	28	6	0	0	2	100
CFU2	41	11	43	2	0	0	3	100
CFU4	41	0	39	14	0	0	6	100
CFSW	52	6	34	2	1	0	6	100
Hei	90	0	9	1	0	0	0	100
Ves	66	3	30	0	1	0	1	100
SS1	67	13	18	0	0	0	3	100
SS2	74	8	18	0	0	0	1	100
SS3	82	4	13	0	0	0	1	100
SS4	78	4	17	0	0	0	1	100
R8D1	68	6	25	0	0	0	2	100
OAP	91	1	6	0	0	0	2	100
PS2	70	17	9	0	1	1	1	100
PS3	63	16	17	0	0	1	3	100
HLA	51	24	24	0	0	0	1	100
MSH	82	6	9	0	1	0	3	100
BT	80	0	14	0	0	5	1	100

g., Christensen et al., 2005; Glotch et al., 2010, 2011; Wray et al., 2013). Feldspars are observed in all samples at concentrations from 8.5–42.5%; no other mineral was ubiquitous (Table 4).

3.2. VNIR spectral results

Fig. 3 shows the 250–125 μm size fraction VNIR spectra for each sample. Fig. 4 shows the maximum-normalized 250–125 μm size fraction VNIR spectra for each sample, offset for clarity. Maximum normalization is applied to the spectra in Fig. 4 to emphasize spectral features that would not otherwise be visible if all spectra were plotted on the sample scale, as some samples (e.g., CFU4) have very low reflectance values (~5–10%).

The VNIR region contains several absorption bands relevant to the

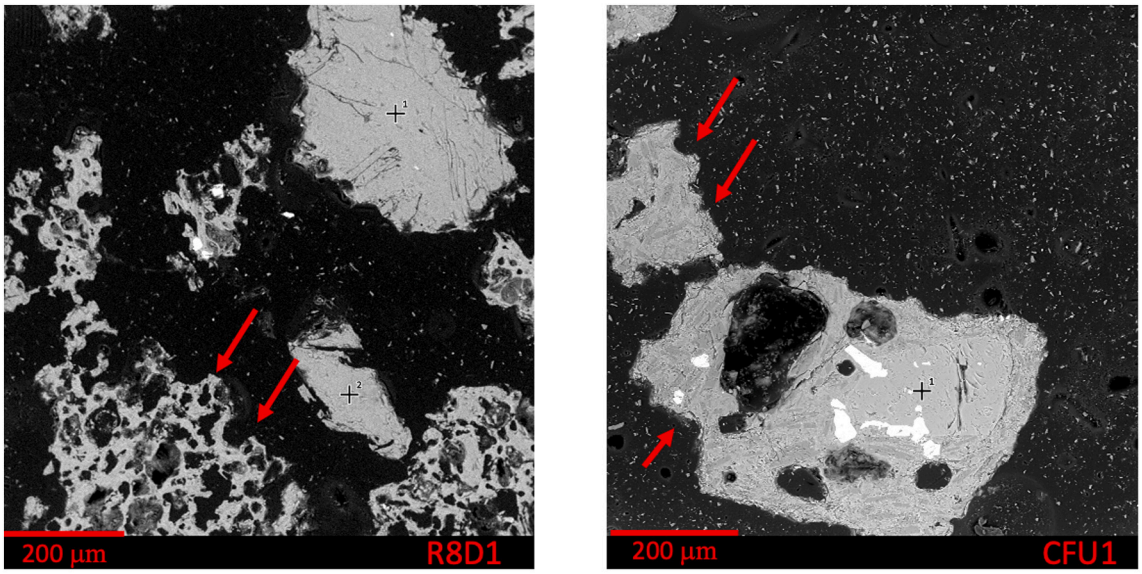

Fig. 1. Example SEM images of a sample without a glassy groundmass (R8D1) and sample with a glassy groundmass (CFU1). Scale bars are 200 µm. Red arrows point to glass. (For interpretation of the references to colour in this figure legend, the reader is referred to the web version of this article.)

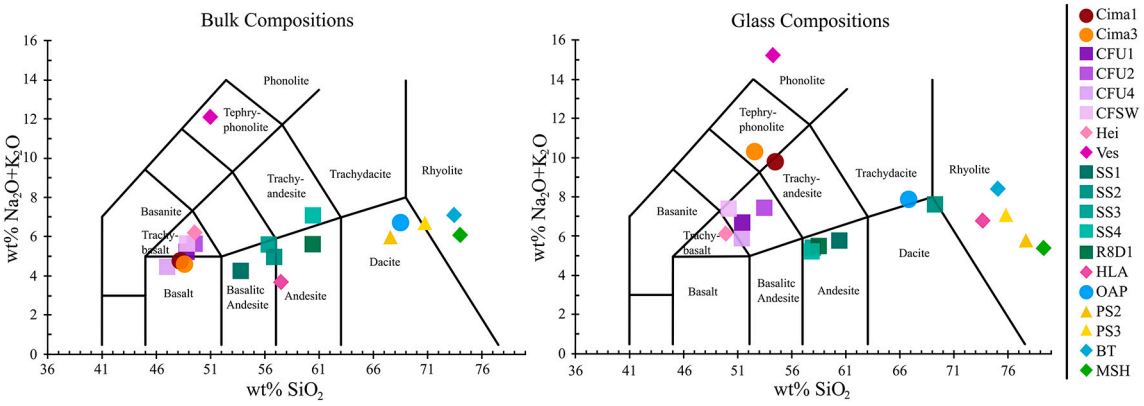

Fig. 2. Total-alkali vs silica (TAS) diagrams showing bulk (left) and glass (right) compositions. Note that bulk and glass compositions differ for every sample.

samples presented here. H_2O and -OH bands occur near 1.4, 1.9, and 2.2 µm (Hunt, 1979; Crown and Pieters, 1987; Clark et al., 1990). In the absence of water, the 1.9 µm feature can be attributed to other atomic bonds such as Fe^{3+} substitution into tetrahedral coordination sites (Adams and Filice, 1967; Crown and Pieters, 1987). Ferrous (Fe^{2+}) and ferric (Fe^{3+}) iron have bands at 0.7 and 1.0 µm (Adams and Filice, 1967; Pieters and Englert, 1993). The presence of ferro-magnesium silicates such as olivine and pyroxene results in absorption features around 1 µm, with the exact shape and position dependent on the mineral composition and abundance (Adams, 1974). Fe-bearing pyroxenes can also produce broad absorption bands at 1.2 and 2 µm (Klima et al., 2007). Plagioclase generally has a high-reflectance VNIR spectrum but can have weak absorptions near 1.2 µm due trace amounts of Fe^{2+} (Cloutis and Gaffey, 1991). The plagioclase 1.2 µm feature is generally overwhelmed by stronger Fe^{2+} bands when other mafic minerals are also present.

Glass, by definition, has no set composition or long-range crystalline structure, which can make spectral analysis difficult. Fe-bearing glass can give broad bands at 0.4–0.65, 1.1, and 2.2 µm (Adams and Filice, 1967; Crisp et al., 1990; Cannon et al., 2017). Glasses can also decrease the albedo of spectra in the VNIR region (Adams and McCord, 1971; Crown and Pieters, 1987). Previous work with basaltic glasses has shown that above 20–30% crystallinity, mineral phases dominate VNIR spectra (Horgan et al., 2014). Eight of the samples presented here has crystallinity <20%, (BT, Hei, OAP, HSM, PS2, SS2, SS3, SS4); none is basaltic, and several samples have glasses containing less than 1 wt% FeO (Tables 3, 4).

No hydrous phases are observed in any significant quantities (e.g., >1%) in any of the samples (Table 4; mineral compositions in supplementary). Therefore, the presence of -OH features in the spectra is unlikely to be due to significant alteration or hydrous-bearing phases. The subtle OH band at 1.9 µm is likely due to minor adsorbed water on the particulate samples. The presence of a minor 2.2 µm band in most VNIR spectra could be due to several origins. Absorptions near 2.2 µm are caused by -O-H bonds, which result from either Si-O-H bonds in glasses (Bartholomew et al., 1980), or -OH bonds to either Al, Fe, or Mg. Features near 2.2 µm are commonly due to phyllosilicate minerals such as kaolinite-serpentinites, (Clark et al., 1990; Bishop et al., 2008), or caused by hydrated aluminosilicates such as allophane or imogolite (Bishop et al., 2013).

Deep absorption bands at 1.4 µm seen in the PS2 and BT spectra could be due to OH^- bonds (Gaffey et al., 1993), unlike the shallower (<5% change in reflectance) absorption bands seen in the other spectra. Because no smectite or other alteration phases are observed (e.g., Table 4), it is unlikely that the 1.4 µm feature is due to a major presence of hydrated mineral phases. PS2 and BT have glass oxide totals below 100 wt% (e.g., a total of 97.2 ± 1.2 wt%, Table 3), and the deepest 1.4

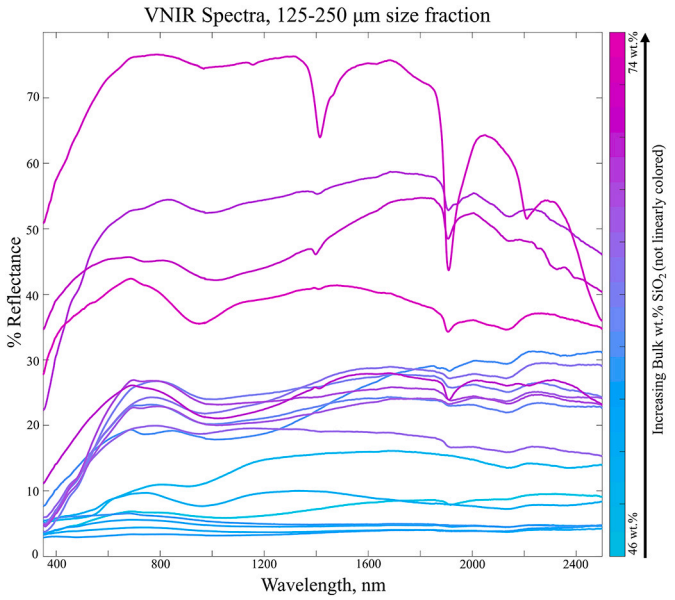

Fig. 3. Representative VNIR spectra from each sample. 125–250 μm size fraction spectra are shown. Spectra are colored by increasing bulk wt% SiO_2. Coloration is not linearly applied to wt% SiO_2 values.

μm (-OH) bands observed (Fig. 3, Fig. 4). All other samples have oxide totals within 1 wt% of 100 wt%. Glass totals can be used to estimate glass volatile concentrations as the difference between a 100% oxide total and the actual oxide total (Devine et al., 1995). The presence of strong -OH spectral features suggest that the low oxide totals may be the result of glass hydration with volatile concentrations of 2.2–2.8 wt% (± >0.7 wt%; Devine et al., 1995).

As bulk SiO_2 wt% increases, the average VNIR reflectance values given in Fig. 3 also increase, consistent with the rising sample albedo with growing SiO_2 content. More felsic samples also tend to have a larger range of reflectance values (e.g., a rhyolitic sample with 74.0 wt% SiO_2 ranges from 37 to 80%, while a basaltic sample with 48.8 wt% SiO_2 ranges from 5 to 20% reflectance). No other trends with oxides or composition are observed in the VNIR region, despite the presence of an Fe^{2+} band near 0.9 μm in some samples.

Sample reflectance changes with size fraction, with the <63 μm having the highest average reflectance (e.g., Fig. 5). This observed trend is consistent with previous research showing that smaller size fractions have increased albedo, and thus reflectance (e.g., Adams and Filice, 1967), though spectral features are not shifted. Different size fractions of a single material can have different spectral feature intensities in the VNIR (Gaffey et al., 1993), which explains the changes in band depth observed between the spectra of different size fractions for each sample (Fig. 5).

3.3. MIR spectral results

Fig. 6 shows the 250–125 μm size fraction MIR spectra for each sample. Fig. 7 shows the spectra without offset to show the full range of spectral variability, while spectra in Fig. 7 are offset for clarity.

Pure-glass MIR spectra are generally featureless compared to the spectra of fully crystalline samples, attributed to the lack of long-range order in glasses (e.g., Minitti et al., 2002; Fu et al., 2017). With as little as 15% crystallinity, individual silicate bond features can be seen over glass signals (Minitti et al., 2002). The Christiansen feature (~1250 cm^{-1}) and the reststrahlen band region (~800–1100 cm^{-1}) result from the primary vibrational modes of the anionic atomic bond vibrations (Si—O and Si-Al-O) in mineral phases (Salisbury and Walter, 1989; Christensen et al., 2000; King et al., 2004). The MIR region also contains

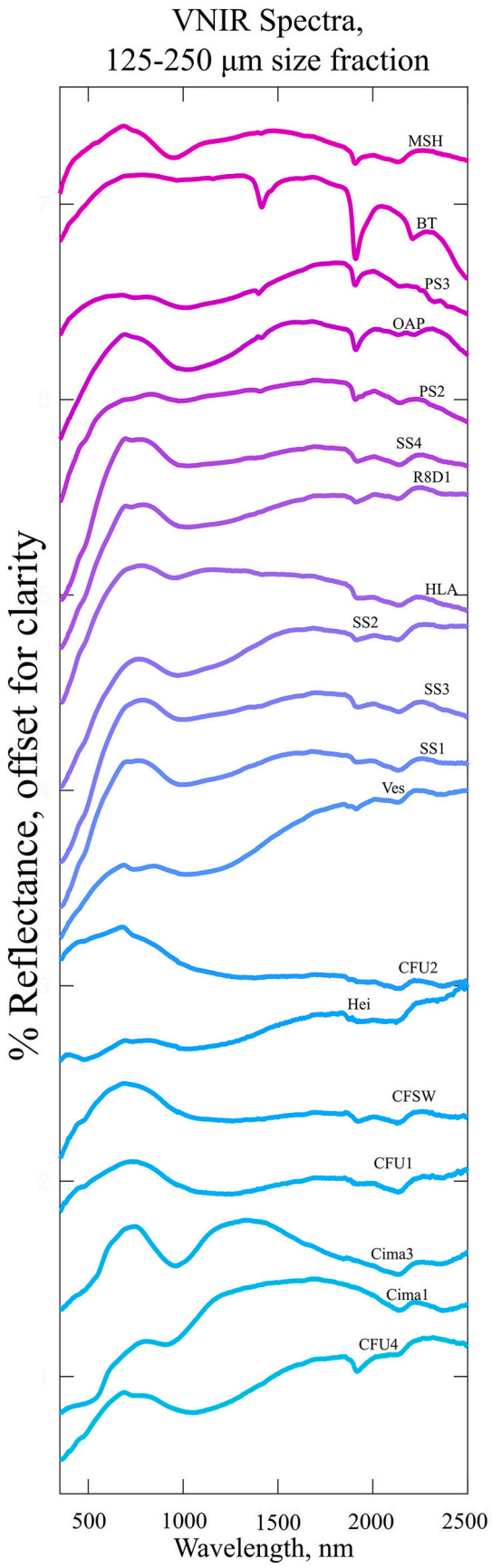

Fig. 4. VNIR 125–250 μm size fraction spectra from each sample, offset for clarity. Spectra are maximum-normalized, and ordered by bulk wt% SiO_2. Coloration matches to Fig. 3.

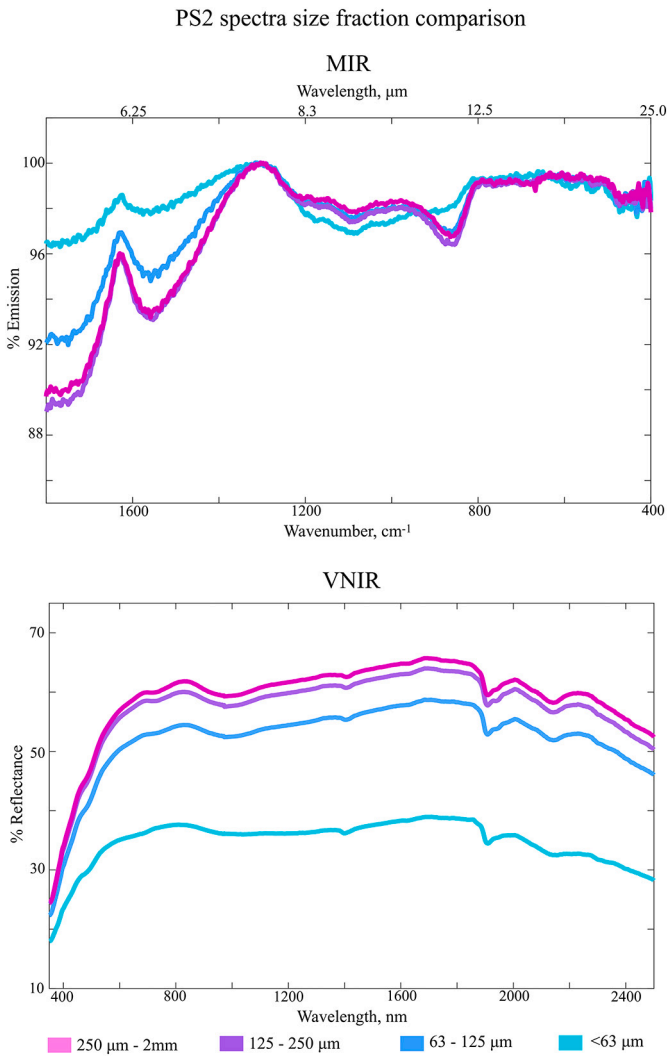

Fig. 5. Comparison of MIR (top) and VNIR (bottom) spectra of the different size fractions of sample PS2.

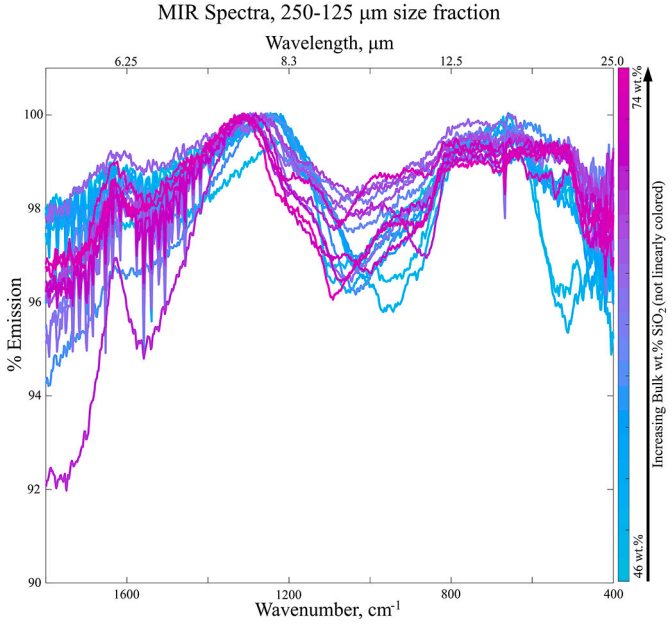

Fig. 6. Representative MIR spectra from each sample. 125–250 μm size fraction spectra are shown. Spectra are colored by increasing bulk wt% SiO_2. Coloration is not linearly applied to wt% SiO_2 values.

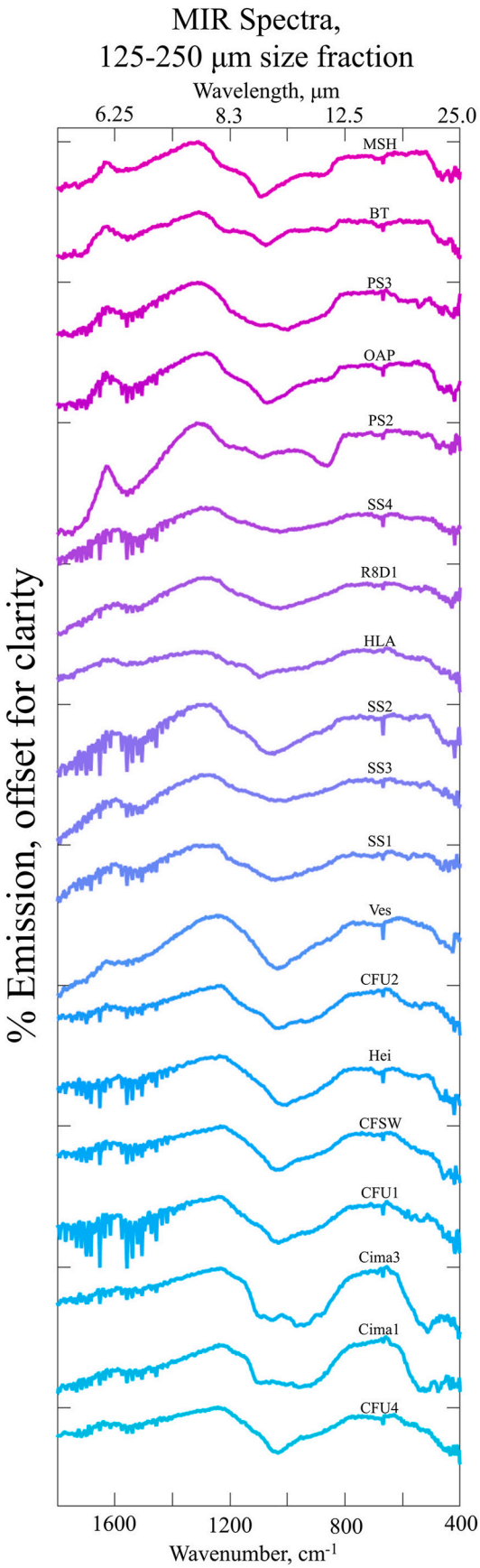

Fig. 7. MIR 125–250 μm size fraction spectra from each sample, offset for clarity. Spectra are ordered by bulk wt% SiO_2. Colors match with Fig. 6.

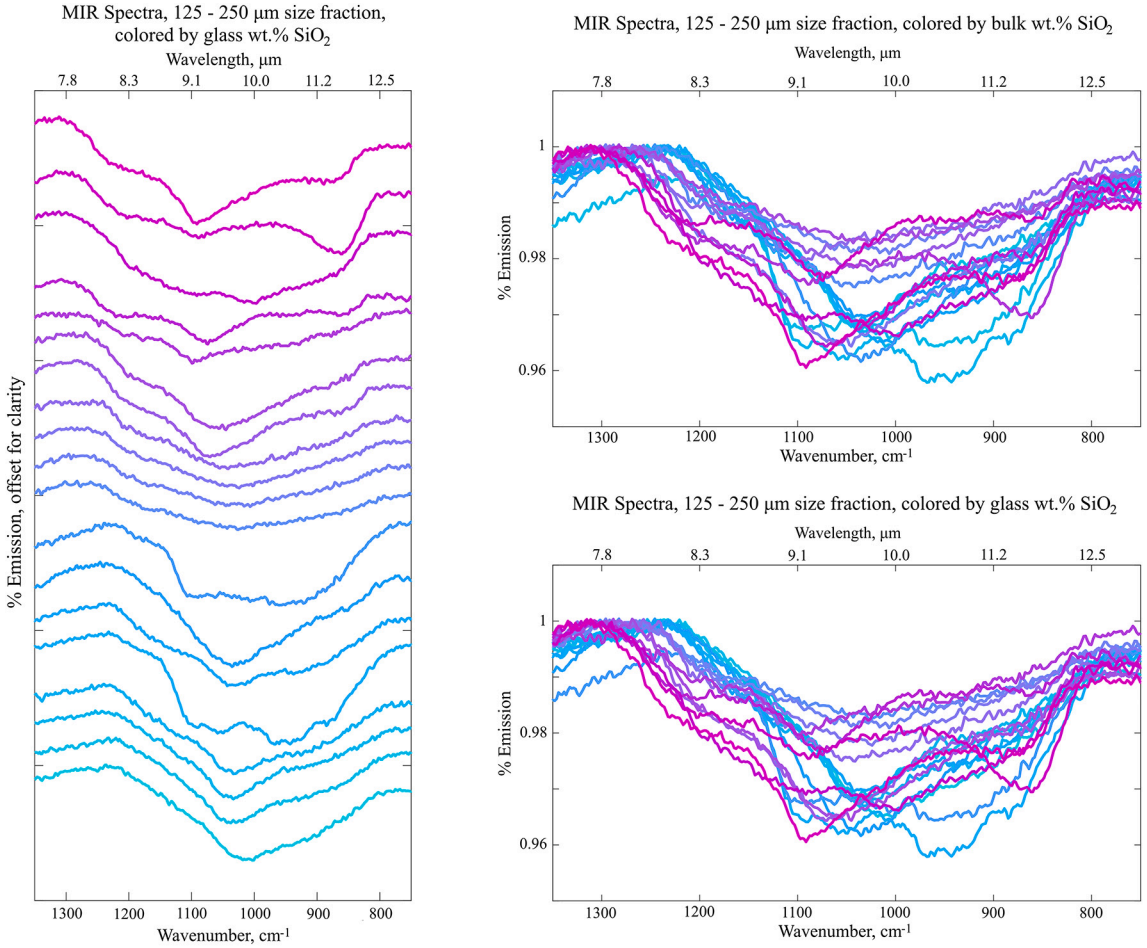

Fig. 8. Trends with composition and the Christensen feature. a) Stacked plot of spectra colored by sample glass wt% SiO_2. b) Spectra colored by bulk wt% SiO_2. c) Spectra colored by glass wt% SiO_2. The same pattern is observed in both a and b.

several different gas absorptions; all spectra presented here have an atmospheric CO_2 absorption at 667 cm^{-1}, as well as atmospheric water absorptions above 1500 cm^{-1}, including the fundamental H2O vibrational feature at ~1600 cm^{-1}. Gas features in the MIR are typically sharp, narrow features, while the silicate features are broader.

The spectra display systematic variation in the emission of a sample's spectrum with size fraction, with the <63 µm size fraction of a sample emitting the least (e.g., Fig. 5). In some samples (e.g., PS2, Fig. 5), smaller size fractions may exhibit new transparency features (e.g., Salisbury and Walter, 1989; Cooper et al., 2002) not seen in the larger (250–500 µm or 250 µm–2 mm) size fractions. These observed trends are consistent with previous research (e.g., Lyon, 1965).

In the MIR (Fig. 8), bulk and glass SiO_2 wt% correlate with the position of the Christiansen feature (e.g., Conel, 1969), so that the feature occurs at higher wavenumbers (shorter wavelengths) with increasing sample wt% SiO_2; this trend is seen with both bulk and glass wt% SiO_2 (Fig. 8b,c). The Christiansen feature is not sensitive to grain size or crystallinity (Salisbury and Walter, 1989; Salisbury and Wald, 1992; Ramsey and Christensen, 1998), which is why the trend is evident despite the inconsistent crystallinity of the samples.

The reststrahlen band region displays multiple minima in most spectra (e.g, Fig. 9a).The reststrahlen band region records Si—O and Si-Al-O bond stretching, with the exact position of the band shifting to reflect the geometry of the tetrahedral Si—O or Si-Al-O bonds (King et al., 2004, references within). The multiple minima observed in our MIR spectra likely result from the different bonds present in the varying mineral and glass phases in the sample. Additionally, glasses can contain several different Si-tetrahedral units due to their amorphous nature, which can further contribute to the presence of multiple minima in the reststrahlen band region (Crisp et al., 1990; King et al., 2004; Dalby and King, 2006).

The changes observed in the reststrahlen band between size fractions of a sample (such as the change in reststrahlen band minimum, Fig. 9b-d) are expected because the reststrahlen band is sensitive to size fraction (Ramsey and Christensen, 1998). The deepest minimum in the reststrahlen band displays a loose positive correlation with glass wt% SiO_2 across all size fractions (Fig. 9b-d). This correlates with previous research (e.g., Hook et al., 2005), though this relationship only holds within individual size fractions >63 µm.

4. Summary and conclusions

This library presents the VNIR and MIR spectra of nineteen tephra samples that span a wide range of explosive volcanic compositions found on Earth. For each sample, the phase assemblage, glass, mineral, and bulk compositions have been described. Crucially, several size fractions

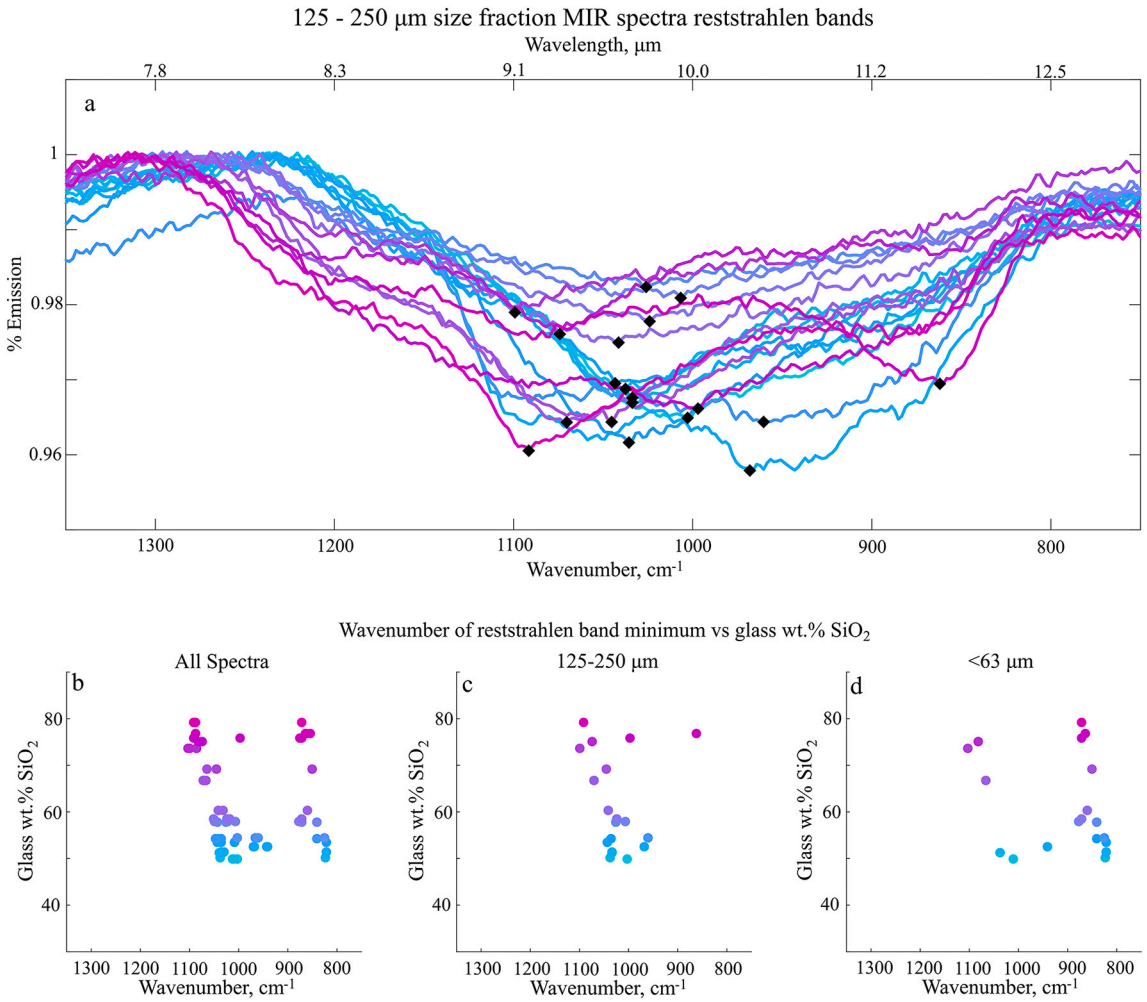

Fig. 9. Trends with the reststrahlen band region. a) Spectra colored by glass wt% SiO_2. Black points show the deepest minimum for each sample. b) Wavenumber of the reststrahlen band minimum vs. sample glass wt% SiO_2 for all spectra. c) Wavenumber of the reststrahlen band minimum vs. sample glass wt% SiO_2 for the 250–125 µm size fraction spectra. d) Wavenumber of the reststrahlen band minimum vs. sample glass wt% SiO_2 for the <63 µm size fraction spectra.

are characterized for each sample to directly measure the effects of particle size and facilitate easier comparison with unknown materials. This catalog will provide more realistic spectral end members to aid in identification of materials, either remote-sensed or collected in situ, believed to contain explosive volcanic components.

Author statement

CL performed VNIR and MIR data collection and processing, sample characterization, and led writing of the manuscript.

MM provided the samples and motivation for the study, and contributed to sample characterization.

TG contributed to MIR data collection and VNIR and MIR processing.

BT contributed to VNIR data collection.

CY contributed to MIR data collection.

M. Darby Dyar contributed to VNIR data collection.

All authors contributed to the writing and revision of the manuscript.

Declaration of Competing Interest

The authors declare that they have no known competing financial interests or personal relationships that could have appeared to influence the work reported in this paper.

Acknowledgements

Many thanks to Allan Patchen for assistance on with collecting EMPA data, Lori Shelton for assistance with obtaining the specifics of the OreXpress, and to Marc Hunter for assistance with publishing these data in the Terrestrial Analog Portal. We also thank Dr. Horgan and the two anonymous reviewers for their edits.

Appendix A. Supplementary data

Supplementary data to this article can be found online at https://doi.org/10.1016/j.rse.2022.112965.

References

Adams, John B., 1974. Visible and near-infrared diffuse reflectance spectra of pyroxenes as applied to remote sensing of solid objects in the solar system. J. Geophys. Res. 79 (32), 4829–4836.

Adams, John B., Filice, Alan L., 1967. Spectral reflectance 0.4 to 2.0 microns of silicate rock powders. J. Geophys. Res. 72 (22), 5705–5715.

Adams, John B., McCord, Thomas B., 1971. Optical properties of mineral separates, glass, and anorthositic fragments from Apollo mare samples. In: Lunar and Planetary Science Conference Proceedings, vol. 2, p. 2183.

Bartholomew, R.F., Butler, B.L., Hoover, H.L., Wu, C.K., 1980. Infrared spectra of a water-containing glass. J. Am. Ceram. Soc. 63 (9–10), 481–485.

Bishop, J.L., Lane, M.D., Dyar, M.D., Brown, A.J., 2008. Reflectance and emission spectroscopy study of four groups of phyllosilicates: smectites, kaolinite-serpentines, chlorites and micas. Clay Miner. 43 (1), 35–54.

Bishop, Janice L., Rampe, Elizabeth B., Bish, David L., Abidin, Zaena L., Baker, Leslie L., Matsue, Naoto, Henmi, Teruo, 2013. Spectral and hydration properties of allophane and imogolite. Clay Clay Miner. 61 (1), 57–74.
Brown, Francis H., Sarna-Wojcicki, Andrei M., Meyer, Charles E., Haileab, Bereket, 1992. Correlation of Pliocene and Pleistocene tephra layers between the Turkana Basin of East Africa and the Gulf of Aden. Quat. Int. 13, 55–67.
Cannon, Kevin M., Mustard, John F., Parman, Stephen W., Sklute, Elizabeth C., Darby Dyar, M., Cooper, Reid F., 2017. Spectral properties of Martian and other planetary glasses and their detection in remotely sensed data. J. Geophys. Res. Planet 122 (1), 249–268.
Carter, Lionel, Nelson, Campbell S., Neil, Helen L., Froggatt, Paul C., 1995. Correlation, dispersal, and preservation of the Kawakawa Tephra and other late Quaternary tephra layers in the Southwest Pacific Ocean. N. Z. J. Geol. Geophys. 38 (1), 29–46.
Cassidy, Michael, Watt, Sebastian F.L., Palmer, Martin R., Trofimovs, Jessica, Symons, William, Maclachlan, Suzanne E., Stinton, Adam J., 2014. Construction of volcanic records from marine sediment cores: a review and case study (Montserrat, West Indies). Earth Sci. Rev. 138, 137–155.
Christensen, Philip R., Bandfield, Joshua L., Hamilton, Victoria E., Howard, Douglas A., Lane, Melissa D., Piatek, Jennifer L., Ruff, Steven W., Stefanov, William L., 2000. A thermal emission spectral library of rock-forming minerals. J. Geophys. Res. Planets 105 (E4), 9735–9739.
Christensen, P.R., McSween Jr., H.Y., Bandfield, J.L., Ruff, S.W., Rogers, A.D., Hamilton, V.E., Gorelick, N., et al., 2005. Evidence for magmatic evolution and diversity on Mars from infrared observations. Nature 436 (7050), 504.
Clark, Roger N., King, Trude V.V., Klejwa, Matthew, Swayze, Gregg A., Vergo, Norma, 1990. High spectral resolution reflectance spectroscopy of minerals. J. Geophys. Res. Solid Earth 95 (B8), 12653–12680.
Clark, Roger N., Swayze, Gregg A., Eric Livo, K., Kokaly, Raymond F., Sutley, Steve J., Brad Dalton, J., McDougal, Robert R., Gent, Carol A., 2003. Imaging spectroscopy: earth and planetary remote sensing with the USGS Tetracorder and expert systems. J. Geophys. Res. Planet 108 (E12).
Cloutis, Edward A., Gaffey, Michael J., 1991. Spectral-compositional variations in the constituent minerals of mafic and ultramafic assemblages and remote sensing implications. Earth Moon Planet. 53 (1), 11–53.
Conel, J.E., 1969. Infrared emissivities of silicates: experimental results and a cloudy atmosphere model of spectral emission from condensed particulate mediums. J. Geophys. Res. 74, 1614–1634.
Cooper, B.L., Salisbury, J.W., Killen, R.M., Potter, A.E., 2002. Midinfrared spectral features of rocks and their powders. J. Geophys. Res. Planet 107 (E4), 1–17.
Crisp, Joy, Kahle, Anne B., Abbott, Elsa A., 1990. Thermal infrared spectral character of Hawaiian basaltic glasses. J. Geophys. Res. Solid Earth 95 (B13), 21657–21669.
Crown, David, Pieters, Carle, 1987. Spectral properties of plagioclase and pyroxene mixtures and the interpretation of lunar soil spectra. Icarus 72 (3), 492–506.
Dalby, Kim N., King, Penelope L., 2006. A new approach to determine and quantify structural units in silicate glasses using micro-reflectance Fourier-Transform infrared spectroscopy. Am. Mineral. 91 (11–12), 1783–1793.
Delano, John W., 1986. Pristine lunar glasses: criteria, data, and implications. J. Geophys. Res. Solid Earth 91 (B4), 201–213.
Devine, Joseph D., Gardner, James E., Brack, Hans P., Layne, Graham D., Rutherford, Malcolm J., 1995. Comparison of microanalytical methods for estimating H_2O contents of silicic volcanic glasses. Am. Mineral. 80 (3–4), 319–328.
Dufresne, Céleste D.M., King, Penelope L., Darby Dyar, M., Dalby, Kim N., 2009. Effect of SiO_2, total FeO, Fe^{3+}/Fe^{2+}, and alkali elements in basaltic glasses on mid-infrared spectra. Am. Mineral. 94 (11–12), 1580–1590.
Fogel, Robert A., Rutherford, Malcolm J., 1995. Magmatic volatiles in primitive lunar glasses: I. FTIR and EPMA analyses of Apollo 15 green and yellow glasses and revision of the volatile-assisted fire-fountain theory. Geochim. Cosmochim. Acta 59 (1), 201–215.
Fu, Xiaohui, Wang, Alian, Krawczynski, Michael J., 2017. Characterizing amorphous silicates in extraterrestrial materials: polymerization effects on Raman and mid-IR spectral features of alkali and alkali earth silicate glasses. J. Geophys. Res. Planet 122 (5), 839–855.
Gaddis, Lisa R., Pieters, Carle M., Ray Hawke, B., 1985. Remote sensing of lunar pyroclastic mantling deposits. Icarus 61 (3), 461–489.
Gaffey, Susan J., McFadden, Lucy A., Nash, Douglas, Pieters, Carle M., 1993. Ultraviolet, visible, and near-infrared reflectance spectroscopy: Laboratory spectra of geologic materials. In: Pieters, Englert (Eds.), Remote Geochemical Analysis: Elemental and Mineralogical Composition. Cambridge University Press, pp. 43–77.
Glotch, T.D., Lucey, P.G., Bandfield, J.L., Greenhagen, B.T., Thomas, I.R., Elphic, R.C., Bowles, N., Wyatt, M.B., Allen, C.C., Donaldson-Hanna, K., Paige, D.A., 2010. Highly silicic compositions on the Moon. Science 329, 1510–1513.
Glotch, Timothy D., Hagerty, Justin J., Lucey, Paul G., Hawke, B. Ray, Giguere, Thomas A., Arnold, Jessica A., Williams, Jean-Pierre, Jolliff, Bradley L., Paige, David A., 2011. The Mairan domes: silicic volcanic constructs on the Moon. Geophys. Res. Lett. 38 (21).
Goudge, Timothy A., Head, James W., Kerber, Laura, Blewett, David T., Denevi, Brett W., Domingue, Deborah L., Gillis-Davis, Jeffrey J., et al., 2014. Global inventory and characterization of pyroclastic deposits on Mercury: new insights into pyroclastic activity from MESSENGER orbital data. J. Geophys. Res. Planet 119 (3), 635–658.
Head, James W., Murchie, Scott L., Prockter, Louise M., Robinson, Mark S., Solomon, Sean C., Strom, Robert G., Chapman, Clark R., et al., 2008. Volcanism on Mercury: evidence from the first MESSENGER flyby. Science 321 (5885), 69–72.
Heiken, Geant H., McKay, David S., Brown, R.W., 1974. Lunar deposits of possible pyroclastic origin. Geochim. Cosmochim. Acta 38 (11), 1703–1718.
Hook, Simon J., Dmochowski, Jane E., Howard, Keith A., Rowan, Lawrence C., Karlstrom, Karl E., Stock, Joann M., 2005. Mapping variations in weight percent silica measured from multispectral thermal infrared imagery—examples from the Hiller Mountains, Nevada, USA and Tres Virgenes-La Reforma, Baja California Sur, Mexico. Remote Sens. Environ. 95 (3), 273–289.
Horgan, Briony, Cloutis, Edward A., Mann, Paul, James, F., 2014. Bell III. "Near-infrared spectra of ferrous mineral mixtures and methods for their identification in planetary surface spectra.". Icarus 234, 132–154.
Hunt, Graham R., 1979. Near-infrared (1.3–2.4) μm spectra of alteration minerals—potential for use in remote sensing. Geophysics 44 (12), 1974–1986.
Hynek, Brian M., Phillips, Roger J., Arvidson, Raymond E., 2003. Explosive volcanism in the Tharsis region: global evidence in the Martian geologic record. J. Geophys. Res. Planet 108 (E9).
Kerber, Laura, Head, James W., Blewett, David T., Solomon, Sean C., Wilson, Lionel, Murchie, Scott L., Robinson, Mark S., Denevi, Brett W., Domingue, Deborah L., 2011. The global distribution of pyroclastic deposits on Mercury: the view from MESSENGER flybys 1–3. Planet. Space Sci. 59 (15), 1895–1909.
King, P.L., McMillan, P.F., Moore, G.M., Ramsey, M., Swayze, G., 2004. Infrared spectroscopy of silicate glasses with application to natural systems. Infr. Spectr. Geochem. Explor. Geochem. Remote Sens. 33, 93–133.
Klima, Rachel L., Pieters, Carlé M., Darby Dyar, M., 2007. Spectroscopy of synthetic Mg-Fe pyroxenes I: spin-allowed and spin-forbidden crystal field bands in the visible and near-infrared. Meteorit. Planet. Sci. 42 (2), 235–253.
Lowe, David J., 2011. Tephrochronology and its application: a review. Quat. Geochronol. 6 (2), 107–153.
Lyon, R.J.P., 1965. Analysis of rocks by spectral infrared emission (8 to 25 microns). Econ. Geol. 60 (4), 715–736.
Mandt, Kathleen E., de Silva, Shanaka L., Zimbelman, James R., Crown, David A., 2008. Origin of the Medusae fossae formation, Mars: insights from a synoptic approach. J. Geophys. Res. Planet 113 (E12).
McCanta, Molly C., Hatfield, Robert G., Thomson, Bradley J., Hook, Simon J., Fisher, Elizabeth, 2015. Identifying cryptotephra units using correlated rapid, nondestructive methods: VSWIR spectroscopy, X-ray fluorescence, and magnetic susceptibility. Geochem. Geophys. Geosyst. 16 (12), 4029–4056.
Minitti, Michelle E., Mustard, John F., Rutherford, Malcolm J., 2002. Effects of glass content and oxidation on the spectra of SNC-like basalts: applications to Mars remote sensing. J. Geophys. Res. Planet 107 (E5), 6–1.
Mustard, John F., Hays, John E., 1997. Effects of hyperfine particles on reflectance spectra from 0.3 to 25 μm. Icarus 125 (1), 145–163.
Nielsen, Charles H., Sigurdsson, Haraldur, 1981. Quantitative methods for electron microprobe analysis of sodium in natural and synthetic glasses. Am. Mineral. 66 (5–6), 547–552.
Parfitt, E.A., Wilson, L., 1995. Explosive volcanic eruptions—IX. The transition between Hawaiian-style lava fountaining and Strombolian explosive activity. Geophys. J. Int. 121 (1), 226–232.
Pieters, Carle M., Englert, Peter A.J., 1993. Remote Geochemical Analysis, Elemental and Mineralogical Composition.
Pieters, Carle, McCord, Thomas B., Charette, Michael P., Adams, John B., 1974. Lunar surface: identification of the dark mantling material in the Apollo 17 soil samples. Science 183 (4130), 1191–1194.
Ramsey, Michael S., Christensen, Philip R., 1998. Mineral abundance determination: quantitative deconvolution of thermal emission spectra. J. Geophys. Res. Solid Earth 103 (B1), 577–596.
Ruff, Steven W., Christensen, Philip R., Barbera, Paul W., Anderson, Donald L., 1997. Quantitative thermal emission spectroscopy of minerals: a laboratory technique for measurement and calibration. J. Geophys. Res. Solid Earth 102 (B7), 14899–14913.
Salisbury, John W., Wald, Andrew, 1992. The role of volume scattering in reducing spectral contrast of reststrahlen bands in spectra of powdered minerals. Icarus 96 (1), 121–128.
Salisbury, John W., Walter, Louis S., 1989. Thermal infrared (2.5–13.5 μm) spectroscopic remote sensing of igneous rock types on particulate planetary surfaces. J. Geophys. Res. Solid Earth 94 (B7), 9192–9202.
Shane, Phil, 2000. Tephrochronology: a New Zealand case study. Earth Sci. Rev. 49 (1–4), 223–259.
Trepte, Charles R., Hitchman, Matthew H., 1992. Tropical stratospheric circulation deduced from satellite aerosol data. Nature 355 (6361), 626–628.
van den Bogaard, Christel, Dörfler, W., Sandgren, P., Schmincke, H.-U., 1994. Correlating the Holocene records: Icelandic tephra found in Schleswig-Holstein (northern Germany). Naturwissenschaften 81 (12), 554–556.
Wilson, Lionel, Head III, James W., 1981. Ascent and eruption of basaltic magma on the Earth and Moon. J. Geophys. Res. Solid Earth 86 (B4), 2971–3001.
Wilson, Lionel, Head III, James W., 1994. Mars: review and analysis of volcanic eruption theory and relationships to observed landforms. Rev. Geophys. 32 (3), 221–263.
Wray, James J., Hansen, Sarah T., Dufek, Josef, Swayze, Gregg A., Murchie, Scott L., Seelos, Frank P., Skok, John R., Irwin III, Rossman P., Ghiorso, Mark S., 2013. Prolonged magmatic activity on Mars inferred from the detection of felsic rocks. Nat. Geosci. 6 (12), 1013.